

PAPER

Vibration energy harvesters with optimized geometry, design, and nonlinearity for robust direct current power delivery

To cite this article: Wen Cai and Ryan L Harné 2019 *Smart Mater. Struct.* **28** 075040

View the [article online](#) for updates and enhancements.

Vibration energy harvesters with optimized geometry, design, and nonlinearity for robust direct current power delivery

Wen Cai  and Ryan L Harne 

Department of Mechanical and Aerospace Engineering, The Ohio State University, Columbus, OH 43210, United States of America

E-mail: harnel3@osu.edu

Received 14 March 2019, revised 27 April 2019

Accepted for publication 29 May 2019

Published 18 June 2019



CrossMark

Abstract

With an ever-growing Internet-of-things, vibration energy harvesting has attracted broad attention to replace consumable batteries to power the many microelectronic devices. To this end, an energy harvester must deliver the required power to an electrical load over a long time horizon. Yet, design practices for energy harvesters often report strategies based on maximizing output voltage and wide frequency range of operation, which is not directly related to performance-robust functioning. Motivated to provide valuable insight to practical development of vibration energy harvesters, this research develops an analytical modeling framework and optimization technique to guide attention to piezoelectric laminated energy harvesting cantilevers with balanced and robust performance characteristics. The model is numerically and experimentally validated to confirm the efficacy of the optimization outcomes. The results indicate that laminated trapezoidal beam shapes with monostable configuration are the best solution to broaden the frequency range of enhanced dynamic behavior, minimize strain at the clamped beam end, and maximize the output voltage in a rectifier circuit. The results also find that the selection of tip mass may not be highly influential for the overall performance so long as the beam shape, beam length, and placement of nonlinearity-induced magnets are appropriately chosen.

Keywords: laminated piezoelectric beam, multi-objective optimization, vibration energy harvesting, genetic algorithm

(Some figures may appear in colour only in the online journal)

1. Introduction

With an accelerating development of the Internet-of-things (IoT), sustainably powering the vast fleet of low-power wireless devices in our world is on the verge of crisis [1]. With a projected growth of IoT devices upwards of tens of billions by 2020 [2], the excessive reliance on chemical batteries threatens the environment and resilience of the global energy economy. Yet, vibrational energy harvesting suggests a promising solution to meet a portion of the accelerating power supply demand [3]. Optimizing such vibration energy harvester platforms to ensure robust direct current (DC) power when subjected to broadband vibration excitation, and

over a long time horizon, is therefore central to the vision of a sustainable IoT [4].

The fundamental requirement of a vibration energy harvester is to ensure the necessary DC power is delivered to an electrical load. Optimization strategies therefore seek to enable this requirement. A straightforward method to maximize output power is to increase the electromechanical coupling coefficient for a piezoelectric harvester platform, which enhances the conversion efficiency between vibration and electrical energies. Cho *et al* [5] uncovered the influences of residual stress, layering thicknesses, and electrode coverage on the resulting electromechanical coupling coefficient for an optimized thin-film PZT membrane design. Wang and

Wu [6] examined the effects of the piezoelectric patch positioning and size for application on a cantilever beam, to show how power harvesting efficiency could be optimized. Lü *et al* [7] proposed an optimization method by introducing an intrinsic power density scale to reduce the number of parameters for optimizing energy conversion efficiency. Qin *et al* [8] investigated the influence of dimensions on the PZT-5A material and arrived at an optimal electromechanical coupling coefficient (k_{15}) for the shear vibration mode of energy harvesting. In addition, after identifying the superiority of a trapezoidal piezoelectric beam shape for mechanical robustness and long service life [9], alternative tapered beam shapes have been studied to enhance the uniformity of strain distribution along the beam length [10–14]. Dietl and Garcia [15] developed an optimization tool on the basis of such trends and proposed an optimal curved piezoelectric beam shape for more uniform strain distribution. Further approaches to the beam configuration have been considered for the sake of maximizing electrical power generation, for example a tapered beam with cavity [16], right-angle piezoelectric cantilevers having auxiliary beams [17], beams with initial curvature [18], and piezoelectric energy harvesters having cellular honeycomb structures [19].

Because linear dynamic response only ensures high output power around the primary resonant frequencies, robust electrical power delivery must involve an energy harvester exhibiting large amplitude dynamic behaviors when subjected to broadband frequency vibration excitation. One well-known method to broaden the frequency range of a piezoelectric energy harvester is to introduce nonlinear magnetic effects [20–22]. Erturk and Inman [23] suggested as much as an 800% increase in output power could be achieved for a bistable magnetopiezoelectric harvester under harmonic vibration when the platform was interfaced with a purely resistive electrical load. Comparatively, Ferrari *et al* [24] reported a 250% increase in output power for a magnetoelastic energy harvester subjected to wideband stochastic excitation. The frequency range for large amplitude response and large output power has been extended also by adopting adaptive bistable harvester designs to more often realize the snap-through behavior [25–27]. In this spirit, Zhou *et al* [28] proposed a flexible bistable energy harvester with two elastic beams to create a variable repulsive magnetic force, which may reduce the potential barrier that must be overcome to ensure snap-through oscillation. Recently instead of focusing on the bistable system, multi-stable systems, such as tri-stable energy harvester, have been introduced to enhance the frequency range and output power achieved for the large amplitude dynamic behaviors [29, 30]. Because the alternating current output from the harvester must be rectified to DC to power electronic devices, nonlinear harvester platforms interfaced with rectifier circuits [31] or power management circuits [32] have also demonstrated broadband frequency response despite interfacing with such nonlinear electrical circuits.

Yet, enhanced dynamic behavior may correspondingly be detrimental to the long working life of the vibration energy harvester. In particular, the PZT material is exceedingly brittle such that it is vulnerable to damage caused by events resulting

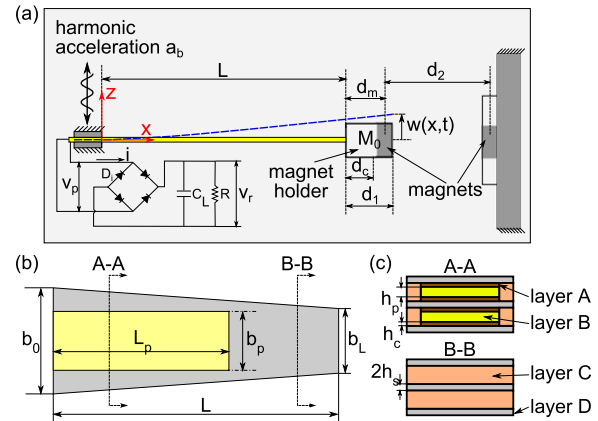


Figure 1. (a) Schematic of nonlinear energy harvester system with repulsive magnets and rectification circuit interface. (b) Dimensions of the piezoelectric beam. (c) Cross-section of the piezoelectric beam among the several layers.

in high bending strain. Without cautious design, a piezoelectric energy harvester could fail in hours, or even in minutes [33–35]. Gundimeda *et al* [36] have helped quantify the mechanical robustness and design flexibility of laminated beams when compared with conventional metal substrates used for piezoelectric beams. Li *et al* [37] further demonstrated the superiority of laminated piezoelectric beams to yield high output power. Yet, strain conditions or laminated beams are seldom considered when optimizing the energy harvester, especially if nonlinearity is introduced.

Given the state-of-the-art in optimization efforts for piezoelectric energy harvesters, a need exists to develop an optimization approach that exploits nonlinearity in the design of custom-shaped harvesters having excellent DC output power, broad frequency range of operation, and exceptional mechanical robustness. This research meets the need via an analytical model and integrated genetic algorithm (GA) optimization framework. The following sections introduce the analytical method, numerically verify the efficacy of the analysis, and then establish the optimization framework. Optimized piezoelectric energy harvesters are then examined and cross-compared, after which an experimental sequence confirms the validity of the theoretical predictions through laboratory examinations. A summary of main discoveries from this research are presented to conclude this report.

2. Analytical model overview

2.1. Analytical model formulation for a laminated piezoelectric beam with magnetic nonlinearity

Figure 1 presents a schematic of the nonlinear energy harvesting system considered in this research. A laminated piezoelectric cantilever is interfaced with a rectifier bridge D_i , smoothing capacitor C_L , and load resistance R , which is a standard energy extraction circuit. The lamination sequence is intricate. As shown in figure 1(b), along the total length L of the clamped beam, the width at the free end b_L and the width

at the fixed end b_0 are the layers D, composed from a glass-reinforced epoxy laminate (FR4). The thickness of the FR4 is $2h_s$. Since ceramic materials are exceedingly difficult to arbitrarily shape due to extreme brittleness, here we consider a piezoelectric PZT-5H layer labeled as layer B that adopts a fixed and commercially available rectangular shape. The subsequent optimization of this report considers other beam design parameters as candidates for optimization, in contrast to change of the PZT-5H layer shape. The length, width, and thickness of the piezoelectric layer considered here are L_p , b_p , and h_p . The two piezoelectric layers shown in figure 1(c) are connected in parallel. The layer A corresponds to a copper electrode layer and has the same length and width as the piezoelectric layer for full electrode coverage. The thickness of the copper layer is h_c . Layer C denotes polyimide that fills the remaining laminate beam volume in the absence of the copper or piezoelectric layers. Repulsive magnets are included to introduce nonlinearity for tuning the frequency response when the cantilever is subjected to the harmonic base acceleration a_b . The total tip mass is taken as M_0 , which constitutes both the magnet as well as the holder required to secure the magnet to the cantilever free tip. The other opposing repulsive magnet is attached to the moving base. In the following derivation, the magnet holder shown in figure 1(a) is assumed to be a rigid extension from the beam tip. The length of the holder is d_1 . The distance between two magnet centers is d_2 .

When the transverse displacement at the free end of the beam is $w(x, t)$, the strain distribution including the nonlinearity [38] caused by the large amplitude vibration is written

$$S_1 = -z[w_{xx}(1 - w_x^2)^{-1/2}] \simeq -zw_{xx}\left(1 + \frac{1}{2}w_x^2\right). \quad (1)$$

The w_x represents for $\frac{\partial w}{\partial x}$, w_{xx} is the corresponding second derivative, z is the distance away from the neutral axis, and S_1 indicates the strain in the x direction caused by deflection in the z axis.

For the piezoelectric layers, the electrical potential $\varphi(z, t)$ is assumed to be a linear function through the respective piezoelectric layer thickness [39, 40]. Therefore

$$E_3 = -\frac{\partial \varphi}{\partial z} = -\varphi_z, \quad (2)$$

where E_3 is the electric field in the z direction. Then, the coupling between mechanical and electrical responses for the piezoelectric layers are

$$\begin{bmatrix} D_3 \\ T_1 \end{bmatrix} = \begin{bmatrix} \varepsilon_{33}^s & e_{31} \\ -e_{31} & E_p \end{bmatrix} \begin{bmatrix} E_3 \\ S_1 \end{bmatrix}. \quad (3)$$

The D_3 is the electric displacement through the piezoelectric layer thickness, T_1 and S_1 are the stress and strain in x direction, e_{31} refers to the coupling between the electric field in the z direction and the stress in the x direction, ε_{33}^s is the piezoelectric permittivity at constant strain, E_p is the Young's modulus of the PZT-5H.

Since the rigid magnet holder has a finite length, the kinetic energy of the tip mass T_m is calculated based on the

velocity at the mass center. The distance from the laminated beam end to the mass center of the holder is d_c as shown in figure 1(a)

$$\begin{aligned} T_m &= \frac{1}{2}M_0[\dot{w}(L + d_c, t) + v_b]^2 \\ &= \frac{1}{2}M_0[\dot{w}(L, t) + d_c \cdot \dot{w}_x(L, t) + v_b]^2. \end{aligned} \quad (4)$$

The \dot{w} is the first derivative of the displacement with respect to the time t , v_b is the velocity of the base.

Therefore, the total kinetic energy of the nonlinear system shown in figure 1(a) is given in (5)

$$\begin{aligned} T &= \frac{1}{2} \int_{V_s} \rho_s [\dot{w}(x, t) + v_b]^2 dV \\ &+ \frac{1}{2} \int_{V_p} \rho_p [\dot{w}(x, t) + v_b]^2 dV \\ &+ \frac{1}{2} \int_{V_c} \rho_c [\dot{w}(x, t) + v_b]^2 dV \\ &+ \frac{1}{2} \int_{V_e} \rho_e [\dot{w}(x, t) + v_b]^2 dV + T_m. \end{aligned} \quad (5)$$

Here and after, the subscripts s , p , c , and e refer to the material of FR4, PZT-5H, copper, and polyimide. These subscripts are then used for the following parameters. The ρ and V denote the corresponding material density and the total volume for each material.

The magnetic potential energy caused by the magnets [21, 24, 41] is

$$\begin{aligned} U_m &= -\int F_{mag} dz = -\frac{1}{2}k_1 w^2(L + d_{mc}, t) \\ &- \frac{1}{4}k_3 w^4(L + d_{mc}, t), \end{aligned} \quad (6)$$

where d_{mc} is the distance between the magnet center installed on the beam to the laminated beam end.

The magnet pair shown in figure 1(a) include identical magnets. As such, the coefficients in (6) are

$$\begin{aligned} k_1 &= f_0 d_2^{-5}, \quad k_3 = -2.5f_0 d_2^{-7}, \quad f_0 = 3\tau m^2 / (2\pi), \\ m &= M_a \cdot V_{mag}. \end{aligned} \quad (7)$$

The τ is the permeability constant in vacuum, m is the effective magnetic moment, d_2 is the center-to-center distance between the two repulsive magnets, M_a is the magnetization of the magnet, V_{mag} is the magnet volume.

The total potential energy for the system is supposed to be

$$\begin{aligned} U &= \int_{V_s} \frac{1}{2} S_1 T_1 dV + \int_{V_c} \frac{1}{2} S_1 T_1 dV \\ &+ \int_{V_p} \frac{1}{2} S_1 T_1 dV + \int_{V_e} \frac{1}{2} S_1 T_1 dV \\ &- \int_{V_p} \frac{1}{2} E_3 D_3 dV + U_m, \end{aligned} \quad (8)$$

where the term T_1 refers to the stress in the x direction.

Substituting equations (1), (3) and (6) into (8), the total potential energy is then given by

$$\begin{aligned}
U = & \int_{V_s} \frac{1}{2} E_s [z^2 (w_{xx}^2 + w_{xx}^2 w_x^2)] dV \\
& + \int_{V_c} \frac{1}{2} E_c [z^2 (w_{xx}^2 + w_{xx}^2 w_x^2)] dV \\
& + \int_{V_p} \frac{1}{2} E_p [z^2 (w_{xx}^2 + w_{xx}^2 w_x^2)] dV \\
& + \int_{V_e} \frac{1}{2} E_e [z^2 (w_{xx}^2 + w_{xx}^2 w_x^2)] dV \\
& - \int_{V_p} \frac{1}{2} (E_3)^2 \varepsilon_{33}^s dV \\
& - \int_{V_p} e_{31} E_3 \left[z \left(w_{xx} + \frac{1}{2} w_{xx} w_x^2 \right) \right] dV \\
& - \frac{1}{2} k_1 w^2 (L + d_{mc}, t) - \frac{1}{4} k_3 w^4 (L + d_{mc}, t).
\end{aligned} \tag{9}$$

The E indicates the Young's modulus, where the subscripts are those defined for the respective layers.

The external work is composed of two parts: mechanical work due to the external base acceleration a_b and electrical work caused by the electrical field inside the piezoelectric layers

$$\begin{aligned}
W = & \int_{V_s} \rho_s a_b w dV + \int_{V_c} \rho_c a_b w dV \\
& + \int_{V_p} \rho_p a_b w dV + \int_{V_e} \rho_e a_b w dV \\
& + M_0 a_b w (L + d_c) - \sum_{q=1}^2 Q_q \cdot v_q.
\end{aligned} \tag{10}$$

The Q_q is the charge in piezoelectric layer q , v_q represents the voltage at the piezoelectric electrodes. Since there are two piezoelectric layers, q ranges from 1 to 2 in this study.

Although there is discontinuity along the beam axis where the piezoelectric layers end, only the fundamental out-of-plane bending mode is dominant in the responses analysis as justified in section 2.2. This motivates the use of the Ritz method in the process to obtain the Euler–Lagrange equations of motion. Suitable trial functions in the assumed solution by the Ritz method ensure that the essential boundary conditions are satisfied for convergence of the approximate solution to the accurate result, including the discontinuity [42].

Assuming that the harmonically forced mechanical and electrical behaviors are respectively separable in space and time, the system dynamics may be approximated as a linear combination of linearly independent trial functions and generalized coordinates. For the mechanical responses, it is assumed that

$$\begin{aligned}
w(x, t) = \boldsymbol{\psi}(x) \mathbf{r}(t) &= \begin{bmatrix} \psi_1(x) & \cdots & \psi_M(x) \end{bmatrix} \begin{bmatrix} r_1(t) \\ \vdots \\ r_M(t) \end{bmatrix} \\
&= \sum_{i=1}^M \psi_i r_i,
\end{aligned} \tag{11}$$

where M is the total number of trial functions assumed in the summation (which is 3 in the following model development), and $r_i(t)$ is the unknown generalized coordinate. The trial functions $\psi_i(x)$ are approximated by the normal modes of a clamped beam with tip mass given in equation (12)

$$\psi_i(x) = \cos \frac{\lambda_i}{L} x - \cosh \frac{\lambda_i}{L} x + \zeta_i \left(\sin \frac{\lambda_i}{L} x - \sinh \frac{\lambda_i}{L} x \right) \tag{12}$$

$$\zeta_i = \frac{\sin \lambda_i - \sinh \lambda_i + \lambda_i \frac{M_0}{M_b} (\cos \lambda_i - \cosh \lambda_i)}{\cos \lambda_i + \cosh \lambda_i - \lambda_i \frac{M_0}{M_b} (\sin \lambda_i - \sinh \lambda_i)}. \tag{13}$$

The M_b is the mass of the beam, λ_i is related to the natural frequency of the system, which can be solved by the transcendental equation (14)

$$\begin{aligned}
1 + \cos \lambda \cosh \lambda + \lambda \frac{M_0}{M_b} (\cos \lambda \sinh \lambda - \sin \lambda \cosh \lambda) \\
= 0.
\end{aligned} \tag{14}$$

The electrical potential is assumed to vary linearly through the thickness of a piezoelectric layer and become zero-valued outside the piezoelectric domains [15, 40]. The normalized voltage at the electrodes existing at $z = h_s + h_p + h_c$ and $z = -(h_s + h_p + h_c)$ are assumed to be 1 and -1 , respectively, given the mirrored positions of the electrodes considering the laminate sequence about the middle plane of the beam. Consequently, the normalized linear distribution of electrical potential through the thickness of the piezoelectric layers is given by equations (16) and (17). The Ritz expansion of the electrical potential for the laminated beam is therefore given in equation (15). The signs of the trial functions of (16) and (17) are opposite since the locations of the piezoelectric layers are mirrored about the middle plane of the laminated beam.

$$\varphi(z, t) = \boldsymbol{\Phi}(z) \mathbf{v}(t) = \begin{bmatrix} \Phi_1(z) & \Phi_2(z) \end{bmatrix} \begin{bmatrix} v_1(t) \\ v_2(t) \end{bmatrix} = \sum_{q=1}^2 \Phi_q v_q \tag{15}$$

$$\Phi_1(z) = \begin{cases} \frac{z - h_s - h_c}{h_p}; & h_s + h_c \leq z \leq h_s + h_p + h_c \\ 0 & \text{elsewhere} \end{cases} \tag{16}$$

$$\Phi_2(z) = \begin{cases} -\frac{z + h_s + h_c}{h_p}; & (h_s + h_p + h_c) \leq z \leq -h_s - h_c \\ 0 & \text{elsewhere.} \end{cases} \tag{17}$$

Here v_q represents the voltage at the electrode of the piezoelectric layer q .

Substituting equations (2), (11), and (15) into the (5), (9), and (10), and then applying the Euler–Lagrange equation (18) with respect to the mechanical or electrical generalized coordinates, which are represented by ξ_m , the governing equations for the nonlinear energy harvesting system are

obtained as shown in equation (19). Here, Rayleigh proportional damping is assumed and nonlinear coupling between the mechanical and electrical dynamics are neglected

$$\frac{\partial}{\partial t} \left[\frac{\partial(T - U + W)}{\partial \dot{\xi}_m} \right] - \frac{\partial(T - U + W)}{\partial \xi_m} = 0 \quad (18)$$

$$[M]\ddot{\mathbf{r}} + [D]\dot{\mathbf{r}} + [K]\mathbf{r} + [K_1]\mathbf{r} + \mathbf{F}_{\text{NL}} + [\Theta]\mathbf{v} = \mathbf{f}_m \quad (19a)$$

$$-[\Theta]\dot{\mathbf{r}} + [C_p]\dot{\mathbf{v}} + [i_p] = 0. \quad (19b)$$

The nonlinear term is given in (20) and $[i_p]$ is the current through the piezoelectric layer.

$$[\mathbf{F}_{\text{NL}}]_m = \sum_{i=1}^M \sum_{j=1}^M \sum_{k=1}^M [K_3]_{mijk} r_{mi} r_{mj} r_{mk}. \quad (20)$$

The matrices in equation (19) are listed in equation (21)

$$\begin{aligned} [M]_{mi} &= \int_{V_s} \rho_s \psi_m \psi_i dV + \int_{V_c} \rho_c \psi_m \psi_i dV \\ &+ \int_{V_p} \rho_p \psi_m \psi_i dV + \int_{V_e} \rho_e \psi_m \psi_i dV \\ &+ M_0 \left(\psi_m|_{x=L} + d_c \frac{\partial \psi_m}{\partial x} \Big|_{x=L} \right) \\ &\times \left(\psi_i|_{x=L} + d_c \frac{\partial \psi_i}{\partial x} \Big|_{x=L} \right) \end{aligned} \quad (21a)$$

$$\begin{aligned} [K]_{mi} &= \int_{V_s} E_s z^2 \left[\frac{d^2 \psi_m}{dx^2} \frac{d^2 \psi_i}{dx^2} \right] dV \\ &+ \int_{V_c} E_c z^2 \left[\frac{d^2 \psi_m}{dx^2} \frac{d^2 \psi_i}{dx^2} \right] dV \\ &+ \int_{V_p} E_p z^2 \left[\frac{d^2 \psi_m}{dx^2} \frac{d^2 \psi_i}{dx^2} \right] dV \\ &+ \int_{V_e} E_e z^2 \left[\frac{d^2 \psi_m}{dx^2} \frac{d^2 \psi_i}{dx^2} \right] dV \end{aligned} \quad (21b)$$

$$[D]_{mi} = \alpha [M]_{mi} + \beta [K]_{mi} \quad (21c)$$

$$\begin{aligned} [K_1]_{mi} &= -k_1 \left(\psi_i|_{x=L} + d_{mc} \frac{\partial \psi_i}{\partial x} \Big|_{x=L} \right) \\ &\times \left(\psi_m|_{x=L} + d_{mc} \frac{\partial \psi_m}{\partial x} \Big|_{x=L} \right) \end{aligned} \quad (21d)$$

$$[\Theta]_{mq} = - \int_{V_p} e_{31z} \frac{d\Phi_q}{dz} \frac{d^2 \psi_m}{dx^2} dV \quad (21e)$$

$$\begin{aligned} [K_3]_{mijk} &= \int_{V_s} E_s z^2 \left(\frac{d^2 \psi_i}{dx^2} \frac{d\psi_j}{dx} \frac{d\psi_k}{dx} \frac{d^2 \psi_m}{dx^2} \right. \\ &\quad \left. + \frac{d^2 \psi_i}{dx^2} \frac{d^2 \psi_j}{dx^2} \frac{d\psi_k}{dx} \frac{d\psi_m}{dx} \right) dV \\ &+ \int_{V_c} E_c z^2 \left(\frac{d^2 \psi_i}{dx^2} \frac{d\psi_j}{dx} \frac{d\psi_k}{dx} \frac{d^2 \psi_m}{dx^2} \right. \\ &\quad \left. + \frac{d^2 \psi_i}{dx^2} \frac{d^2 \psi_j}{dx^2} \frac{d\psi_k}{dx} \frac{d\psi_m}{dx} \right) dV \\ &+ \int_{V_p} E_p z^2 \left(\frac{d^2 \psi_i}{dx^2} \frac{d\psi_j}{dx} \frac{d\psi_k}{dx} \frac{d^2 \psi_m}{dx^2} \right. \\ &\quad \left. + \frac{d^2 \psi_i}{dx^2} \frac{d^2 \psi_j}{dx^2} \frac{d\psi_k}{dx} \frac{d\psi_m}{dx} \right) dV \\ &+ \int_{V_e} E_e z^2 \left(\frac{d^2 \psi_i}{dx^2} \frac{d\psi_j}{dx} \frac{d\psi_k}{dx} \frac{d^2 \psi_m}{dx^2} \right. \\ &\quad \left. + \frac{d^2 \psi_i}{dx^2} \frac{d^2 \psi_j}{dx^2} \frac{d\psi_k}{dx} \frac{d\psi_m}{dx} \right) dV \\ &- k_3 \left(\psi_i|_{x=L} + d_{mc} \frac{\partial \psi_i}{\partial x} \Big|_{x=L} \right) \\ &\times \left(\psi_j|_{x=L} + d_{mc} \frac{\partial \psi_j}{\partial x} \Big|_{x=L} \right) \\ &\times \left(\psi_k|_{x=L} + d_{mc} \frac{\partial \psi_k}{\partial x} \Big|_{x=L} \right) \\ &\times \left(\psi_m|_{x=L} + d_{mc} \frac{\partial \psi_m}{\partial x} \Big|_{x=L} \right) \end{aligned} \quad (21f)$$

$$\begin{aligned} [\mathbf{f}_m]_m &= \int_{V_s} \rho_s a_b \psi_m dV + \int_{V_c} \rho_c a_b \psi_m dV \\ &+ \int_{V_p} \rho_p a_b \psi_m dV + \int_{V_e} \rho_e a_b \psi_m dV \\ &+ M_0 a_b \left(\psi_m|_{x=L} + d_c \frac{\partial \psi_m}{\partial x} \Big|_{x=L} \right) \end{aligned} \quad (21g)$$

$$[C_p]_{nq} = \varepsilon_3 \int_{V_p} \frac{d\Phi_q}{dz} \frac{d\Phi_n}{dz} dV. \quad (21h)$$

From the governing equations (19), the terms $[K_1]$ and \mathbf{F}_{NL} primarily result from the direct influence of the repulsive magnets. By changing the magnet gap d_2 , the system may take on a monostable or bistable configuration. For a monostable configuration, there is one statically stable equilibrium. According to the influence of the magnet gap on the matrix $[K_1]$, the resonance frequency reduces with decrease of the magnet gap. This trend continues to a point. For still smaller magnet gap d_2 , two stable equilibria occur and the harvester becomes bistable. In this way, the dynamic responses that may occur depend on the amplitude and frequency of the base acceleration. These dynamics responses may be snap-through, aperiodic, and intrawell vibration. The differences among these three kinds vibration are described in [22].

2.2. Solutions to the nonlinear system of governing equations

The two piezoelectric layers are in parallel. As a result, the voltage of each piezoelectric layer satisfies

$$v_1 = v_2 = v_p. \quad (22)$$

The governing equations in equation (19) further simplify to be

$$[M]\ddot{\mathbf{r}} + [D]\dot{\mathbf{r}} + [K]\mathbf{r} + [K_1]\mathbf{r} + \mathbf{F}_{NL} + [\Theta_1]v_p = \mathbf{f}_m \quad (23a)$$

$$-[\Theta_1]^T \dot{\mathbf{r}} + C_{p1}\dot{v}_p = -i, \quad (23b)$$

where $[\Theta_1]$ is electromechanical coupling associated with the generalized coordinates, C_{p1} is the internal capacitance of the piezoelectric beam, i and v_p are the current and voltage in the harvesting circuit as shown in figure 1(a).

The base acceleration that drives the energy harvester is assumed to have moderate amplitude such that nonlinear harmonics are weakly induced. Thus, the displacement response frequency of the beam is assumed to coincide with the base acceleration frequency ω [31, 32]. Therefore, the mechanical response are expressed

$$\mathbf{r}(t) = \mathbf{k}(t) + \mathbf{h}(t) \sin \omega t + \mathbf{g}(t) \cos \omega t. \quad (24)$$

Principles of harmonic or stochastic linearization are then utilized to linearize the governing equations (23), [43, 44]. The linearized governing equations are shown in equation (25)

$$[M]\ddot{\mathbf{r}} + [D]\dot{\mathbf{r}} + ([K] + [K_1] + [K_e]^{(k_3)})\mathbf{r} + [\Theta_1]v_p = \mathbf{f}_m \quad (25a)$$

$$-[\Theta_1]^T \dot{\mathbf{r}} + C_{p1}\dot{v}_p = -i. \quad (25b)$$

The equivalent linear stiffness matrix accounting for the nonlinearity is given in (26)

$$[K_e]_{mh}^{(k_3)} = \left\langle \frac{\partial [\tilde{\mathbf{F}}_{NL1}]_m}{\partial r_h} \right\rangle = \sum_{j=1}^M \sum_{k=1}^M ([K_3]_{mhjk} + [K_3]_{mjhk} + [K_3]_{mkjh}) \times \left[k_j k_k + \frac{1}{2}(h_j h_k + g_j g_k) \right]. \quad (26)$$

The $\langle \rangle$ indicates the mathematical expectation operator.

When a rectifier with an RC circuit interfaces with a forced piezoelectric beam, the voltage across the piezoelectric layer electrodes is calculated by (27) [31]

$$v = \left[\frac{-[\Theta_1]^T \mathbf{g}}{C_{p1}\pi} \sin^2 \beta + \frac{[\Theta_1]^T \mathbf{h}}{2C_{p1}\pi} (2\beta - \sin 2\beta) \right] \sin \omega t + \left[\frac{[\Theta_1]^T \mathbf{h}}{C_{p1}\pi} \sin^2 \beta + \frac{[\Theta_1]^T \mathbf{g}}{2C_{p1}\pi} (2\beta - \sin 2\beta) \right] \cos \omega t \quad (27)$$

$$\beta = \arccos \left(\frac{\pi - 2\omega C_{p1}R}{\pi + 2\omega C_{p1}R} \right). \quad (28)$$

Substituting equations (24) and (27) into the governing equation (25), the coefficients for the sinusoidal terms in equation (24) are found from the equations (29) and (30).

$$-\omega^2 [M]\mathbf{h} - \omega [D]\mathbf{g} + ([K] + [K_1] + [K_e]^{(k_3)})\mathbf{h} - \frac{\sin^2 \beta}{C_{p1}\pi} [\Theta_1][\Theta_1]^T \mathbf{g} + \frac{(2\beta - \sin 2\beta)}{2C_{p1}\pi} [\Theta_1][\Theta_1]^T \mathbf{h} = 0 \quad (29)$$

$$-\omega^2 [M]\mathbf{g} + \omega [D]\mathbf{h} + ([K] + [K_1] + [K_e]^{(k_3)})\mathbf{g} + \frac{\sin^2 \beta}{C_{p1}\pi} [\Theta_1][\Theta_1]^T \mathbf{h} + \frac{(2\beta - \sin 2\beta)}{2C_{p1}\pi} [\Theta_1][\Theta_1]^T \mathbf{h} = \mathbf{f}_m. \quad (30)$$

By integrating the governing equations (25) over one period of the harmonic excitation force $2\pi/\omega$, the equations for the constant terms \mathbf{k} in equation (24) are obtained, as shown in equation (31)

$$\{[K] + [K_1]\}\mathbf{k} + \boldsymbol{\kappa}^{(k_3)} = 0 \quad (31)$$

$$[\boldsymbol{\kappa}^{(k_3)}]_m = \sum_{i=1}^M \sum_{j=1}^M \sum_{k=1}^M [K_3]_{mijk} k_i k_j k_k + \frac{1}{2}([K_3]_{mijk} + [K_3]_{mjik} + [K_3]_{mjki}) \times k_i [g_j g_k + h_j h_k]. \quad (32)$$

By simultaneously solving the equations (29)–(31), the generalized coordinates are found enabling determination of the physical responses via equations (11) and (15).

For other nonlinear interface circuits, such as buck-boost converter or synchronized switch harvesting on inductor electronic interface, with an expression of the output voltage v_p across the piezoelectric beam determined through the respective derivation [32, 45, 46], the procedures described above may be applied for the responses analysis.

3. Numerical verification and comparison to analysis

In order to verify the accuracy of the approximate analytical solution to the nonlinear system of governing equations, fourth-order Runge–Kutta numerical integration is undertaken for the equation system (23). Due to the potential for multiple steady-state dynamic behaviors, 10 separate simulations are taken using normally distributed and randomly selected initial conditions (i.e. displacements, velocities, and voltages) for each combination of base acceleration and system parameters. The simulation duration is set to be 400 periods of the harmonic excitation to ensure steady-state conditions develop. The parameters of the system are given in tables 1 and 2. The beam length L and gap between repulsive magnets d_2 are taken as the outcomes of the optimization, discussed in detail in section 4, but it is sufficient at this stage to use these key parameters for contrast to the simulation. Cubic magnets with side lengths of 6.35 [mm] are used to introduce nonlinearity. The mass of the magnet and mass of the holder contribute to the total mass at the cantilever tip, which is 15 g. Table 2 provides the properties for layers of the laminate beam. In addition to the nominally optimal parameter combination of harvester beam design studied, additional parameter combinations are examined here to comprehensively verify the analytical model. These four cases involve a combination of 7% increase or decrease in beam length L and 5% increase or decrease in magnet gap d_2 .

Table 3. Analytical and simulation results comparison.

	Case 1		Case 2		Case 3	
	Analysis	Simulation	Analysis	Simulation	Analysis	Simulation
Bandwidth (Hz)	11.86	12.08	9.46	9.52	11.74	11.79
RMS value of rectified voltage (V)	13.87	10.7	13.87	11.52	12.43	10.52
RMS value of strain ($\mu\epsilon$)	420.84	427.65	376.27	378.11	332.62	333.9

The table 3 quantitatively compares the analytical and simulation results from figure 2. The frequency bandwidth shown in table 3 is determined by the frequency range in the harmonic voltage responses over which the voltage amplitude is greater than or equal to one-half of the maximum computed voltage amplitude. The corresponding root mean square (RMS) values are calculated inside this frequency bandwidth.

As shown in table 3, the differences between the analytical and simulation results for the frequency bandwidth of large amplitude dynamics and RMS strain at the clamped end are less than 2%. Based on the derivation in section 2, only the fundamental harmonic term is employed to approximate the system responses, thus neglecting diffusion of energy to higher order harmonics, which contributes to the over-prediction of the rectified RMS voltage by the analysis as seen in table 3. Despite this discrepancy, from figure 2(b) the voltage responses of the first three cases show good agreement for the influence of 5% decrease in magnet gap and 7% decrease in beam length. On the other hand, for the bistable cases (cases 4 and 5) in figure 2(a), the harmonic response and steady state assumptions of analysis lead to less agreement with simulation due to the chaotic responses found by numerical simulation that are unable to be reproduced by the harmonic analysis. At higher frequencies of the base acceleration, figure 2 uniformly reveals good quantitative agreement between simulation and analysis, where the significance of nonlinear response is relatively low.

Overall, comparing with the simulation results, the analytical model captures the main characteristics of the nonlinear mechanical and electrical system for both monostable and bistable configurations resulting from the key parameter shifts of beam length and magnet gap.

4. Optimization for a robust energy harvester system via GA

Multiple attributes of an energy harvesting system contribute to a robust system design for persistent DC power delivery. To understand how to design parameters distinctly participate to yield exceptional overall performance for the laminated piezoelectric cantilever, here a multi-objective, GA optimization method is established and then utilized to scrutinize what combinations of design elements give rise to optimality.

4.1. Multi-objective optimization constraints and objectives

To consider a practical design problem, several overall constraints are set in the exploration of feasible design

parameters. The space to install energy harvesters in application is likely confined [47]. The maximum length L_{\max} , width b_{\max} , and thickness t_{\max} of the maximum operating volume are set to be 70 mm, 40 mm, and 4 mm, respectively. The thickness extent is the most limited since the beam vibrates in this axis. To generally minimize dynamic strain and prolong working life, the peak amplitude of displacement must be limited. Specifically, the global constraints based on these limitations for the optimization are as follow:

1. The sum of the beam length L , holder extension d_1 , and magnet gap d_2 must be less than maximum length L_{\max} .
2. The beam length must be greater than 30 mm and less than 60 mm to warrant assumptions of vibration like a beam in contrast to a plate.
3. The displacement amplitude at the beam tip must be less than $t_{\max}/2$ to not exceed the maximum permitted thickness of the operating volume.
4. The magnet gap d_2 must be less than 20 mm and greater than 5 mm, to minimum unnecessary cases of extreme nonlinearity.
5. The displacement amplitude at the beam tip must be greater than 1 mm, otherwise GA searches use excessive time for irrelevant and poor-performing combinations of design parameters.

The following three objectives are utilized for the multi-objective optimization considered in this report.

1. Frequency range f_{range} . The f_{range} is calculated from the voltage amplitude based on the concept of frequency bandwidth defined in section 3. For a bistable configuration of the energy harvester, only the snap-through response is considered to determine the frequency range.
2. Total RMS of rectified output voltage V_{rms} in f_{range} . For a monostable system, the values inside the frequency range f_{range} are included in the calculation. For a bistable system, only the values associated with snap-through inside the frequency range contribute to the cost function of V_{rms} .
3. Total RMS of strain at the clamped beam end on the bottom surface S_{rms} in f_{range} . The calculation is similar to the procedures described in the objective 2. The difference occurs when the system becomes bistable. Because the existence of non-zero static equilibrium positions will cause residual strain in the whole frequency range. The RMS strain for bistable configurations include the contributions from the residual strain and the dynamic strain amplitude.

The multi-objective optimization is formally defined by a weighted sum of the individual objectives [48]. A non-dimensionalization is applied before the summation of components. The linear response for a piezoelectric cantilever is adopted to obtain the non-dimensionalization constants. Since the bandwidth for a linear response is narrow when compared to the nonlinear dynamic behavior, the resonance frequency f_0 of the linear piezoelectric cantilever is used to normalize the f_{range} . The voltage V_0 at resonance for the linear piezoelectric cantilever is used to normalize V_{rms} . Finally, the strain S_0 at the fixed end on the bottom surface of the linear piezoelectric cantilever at resonance is used to normalize S_{rms} . These values are found to be

$$f_0 = 25 \text{ Hz}, V_0 = 65 \text{ V}, S_0 = 1365 \mu\epsilon. \quad (33)$$

The total objective employed for optimization is

$$\text{cost} = -w_f \frac{f_{range}}{f_0} - w_v \frac{V_{rms}}{V_0} + w_s \frac{S_{rms}}{S_0} \quad (34)$$

$$w_f + w_v + w_s = 1. \quad (35)$$

The w_f , w_v , and w_s are respectively weights for the objectives of frequency range, rectified output voltage, and strain condition. Since an energy harvester can deliver high output power in a wide frequency range with a reasonable low strain condition is preferred, with the total objective defined in equation (34), the smallest value of the total objective indicates the optimal design.

The GA optimization developed for this research is inspired through the specific strategies described in Haupt and Haupt [48]. A total of 100 generations including populations with 80 individuals are used for broad evaluation of the parameter space. Each individual is a combination of the design parameters defined for the several optimization studies considered in the following sections. Each individual is evaluated for the three distinct objectives: frequency range, RMS voltage, and RMS strain. The cost function for each individual is then computed by equation (34) according to the multi-objective weighting. The initial population of 80 individuals is generated through random selection inside the constraint range of each design parameter. After evaluating and ranking each individual in the population on the basis of cost function value, the best 50% of the population is selected as parents to generate 40 offspring for the next generation. The remaining 50% of the next generation is the best 50% of the prior population. A mutation rate of 20% is also included to randomly mutate 20% of the next generation to ensure the diversity inside each population.

In the following sections unless otherwise indicated, the parameters given in tables 1 and 2 are employed. The base acceleration frequency range is from 10 to 40 Hz with a constant amplitude 5 ms^{-2} , which is a characteristic of ambient vibrations in heavy industry or automotive applications. Three optimization studies are undertaken to uncover the origins of optimal robust DC power delivery from the laminated piezoelectric cantilever to a fixed load condition. The detailed influence of the resistance on the performance of the piezoelectric energy harvester may be found in [32, 49].

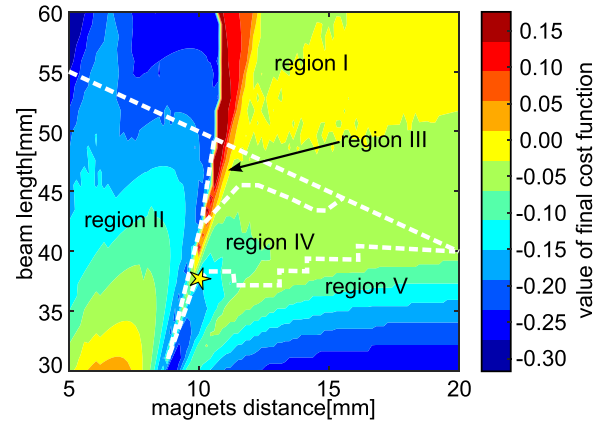


Figure 3. Cost function values of different combination of beam length and magnet gap.

4.2. Optimization results and discussion

4.2.1. Optimization 1: beam length L and magnet gap d_2 . A first optimization problem with the design parameters of beam length L and distance between repulsive magnets d_2 is considered to understand how the nonlinear forces associated with magnetic repulsion influence the ideal energy harvesting beam design.

When the multi-objective cost function weights w_f , w_v , and w_s are the same value ($1/3$), a system with beam length $L = 37.95 \text{ mm}$ and magnet gap $d_2 = 10.17 \text{ mm}$ is identified as optimal. This parameter combination is shown as the star marker in figure 3. Figure 3 presents the values of the cost function as the shading for a wide range of combinations of beam length and magnet gap. Region I conflicts with constraint 1. Regions II and V are neglected because they violate constraint 5. For harvesters designs in region II, with the decrease of the magnet gap, more energy is demanded to pass the potential barrier to realize snap-through behavior. Therefore, in region II only small amplitude of intrawell behaviors are possible. Because of the residual stress caused by the non-zero static equilibria, the intrawell responses result in large strain and low output voltage. For designs inside region V, the resonance frequency of the system lies sufficiently outside the frequency range of interest in this research, which results in low rectified output voltage flow. In contrast, region III includes the designs with displacement amplitude larger than 2 mm, which compromises longevity of the harvester and conflicts with the volumetric space constraints. The star label resides in the region IV, where all combinations of the magnet distance and beam length satisfy the optimization constraints.

The results of this optimization may be assessed in relation to the findings from the numerical verification of the analytical model in figure 2. The case 1 in figure 2 provided the optimal result obtained in this section 4.2.1 optimization when all weights are the same. For cases 4 and 5, the length of the laminated cantilever is increased or the magnet gap is decreased, enhancing the nonlinear interaction between repulsive magnets and causing bistability. The bistability is seen to result in high strain at the clamped end of the

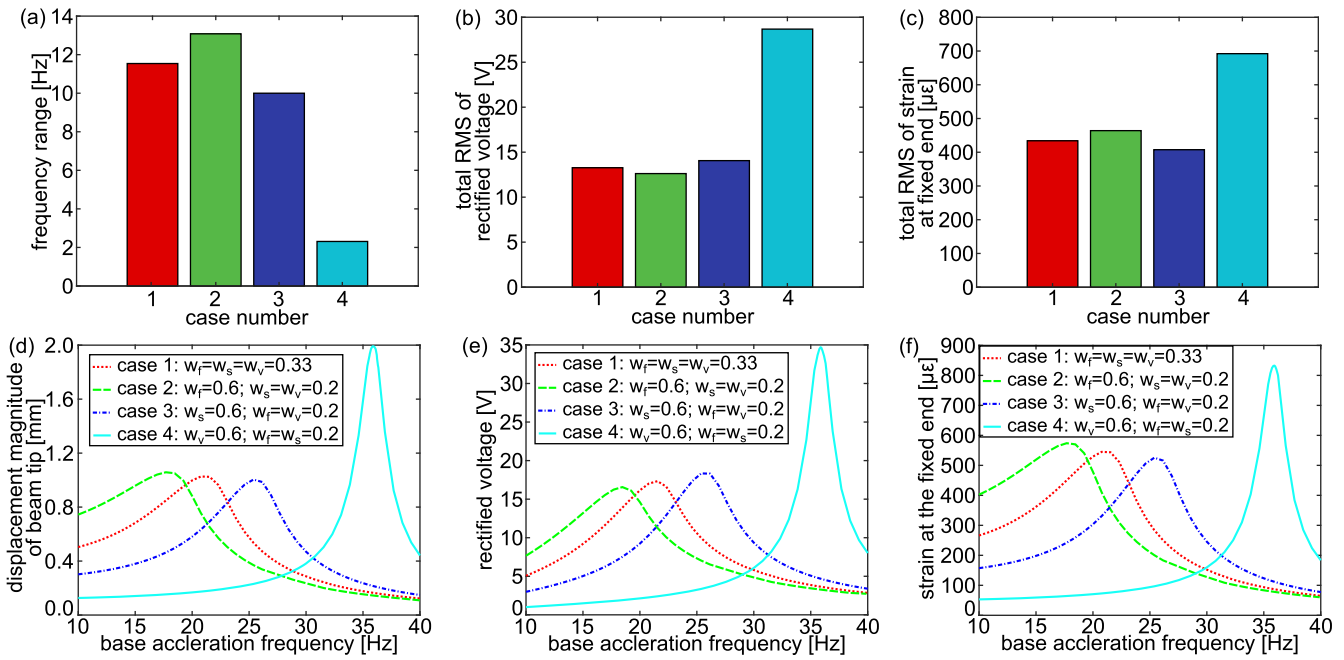


Figure 4. Cost function values of (a) frequency range, (b) total RMS of the rectified output voltage inside the frequency range, and (c) total RMS of the strain at the fixed end on the bottom surface inside the frequency range. Corresponding responses of (d) displacement amplitude of the beam tip, (e) rectified output voltage, and (f) strain at the fixed end on the bottom surface.

cantilever figure 2(c), which practically reduces the working life of the harvester due to the susceptibility to early failure.

The optimal design case 1 and the sub-optimal designs of cases 2 and 3 are monostable, such that the resting equilibria have zero displacement of the beam tip. The findings of figure 2 thus show that a decrease in beam length or increase in magnet gap is desirable to sustain a monostable, and therefore long-life platform design, if the optimal design parameters are unable to be perfectly achieved.

In order to study the influence of weights in this optimization problem, three more optimization problems are considered. Here, the weights assigned to compute the cost function values are differed. Case 2 corresponds to the case that w_f , w_v , and w_s are respectively 0.6, 0.2, and 0.2. Case 3 corresponds to the case that w_f , w_v , and w_s are respectively 0.2, 0.2, and 0.6 for w_f , w_v , and w_s . Finally, case 4 corresponds to the case that w_f , w_v , and w_s are respectively 0.2, 0.6, and 0.2. These unique cases make the individual cost function objectives relatively dominant: (case 2) frequency range f_{range} , (case 3) strain condition S_{rms} , and (case 4) rectified voltage V_{rms} .

The optimal designs identified for the three cases are respectively $L = 37.37$ mm, $d_2 = 9.94$ mm for case 2, $L = 38.38$ mm, $d_2 = 10.51$ mm for case 3, and $L = 43.86$ mm, $d_2 = 16.13$ mm for case 4. Figures 4(a)–(c) present the cost function values computed for harvesters optimized with the different weighted cases. Figures 4(d)–(f) respectively show the responses of beam tip displacement, rectified voltage, and strain at the cantilever end of four cases. Since the magnet gap is more influential in introducing nonlinearity, when the frequency range is dominant (case 2) in the optimization, a smaller magnet gap is optimized to introduce greater nonlinearity that leads to a wider frequency range. Comparatively, when the strain condition is

dominant (case 3), the magnet gap increases to realize the nonlinear resonant behaviors at a comparatively higher frequency as shown in figure 4(d). The responses of the cases 1, 2, and 3 in figures 4(e) and (f) indicate an increase in output voltage at high frequencies of base acceleration due to a shifting of the nonlinear resonance to higher frequencies even with a smaller strain at the cantilever end. This explains why the optimal magnet gap in case 3 is greater than those for cases 1 and 2. For a similar reason, when the voltage is dominant (case 4), the magnet gap is further increased with a much longer beam length to highly increase the rectified output voltage by increased resonant frequency. In comparison with the other three cases, the case 4 optimization demonstrates a tremendous drop in frequency range and increase in strain and output voltage in figures 4(a)–(c). From the responses shown in figure 4(d), the optimal design in case 4 is more similar to a linear configuration for its narrow bandwidth, which illustrates the sensitivity of the voltage objective to the weights change.

4.2.2. Optimization 2: beam length L , magnet gap d_2 , and beam width at free end b_L . Multiple investigations have concluded that a trapezoidal shape for a piezoelectric cantilever results in more uniform strain distribution and often increase in output power [9, 15]. Therefore, the beam width at the free end b_L of the laminated piezoelectric cantilever is introduced as an additional design variable for the optimization. The additional constraint for b_L is that it may vary from zero to the maximum width value, which is 40 mm as stated in section 4.1. Four optimization cases, having the same variation of objective weights employed in section 4.2.1, are considered here. As in section 4.2.1, these

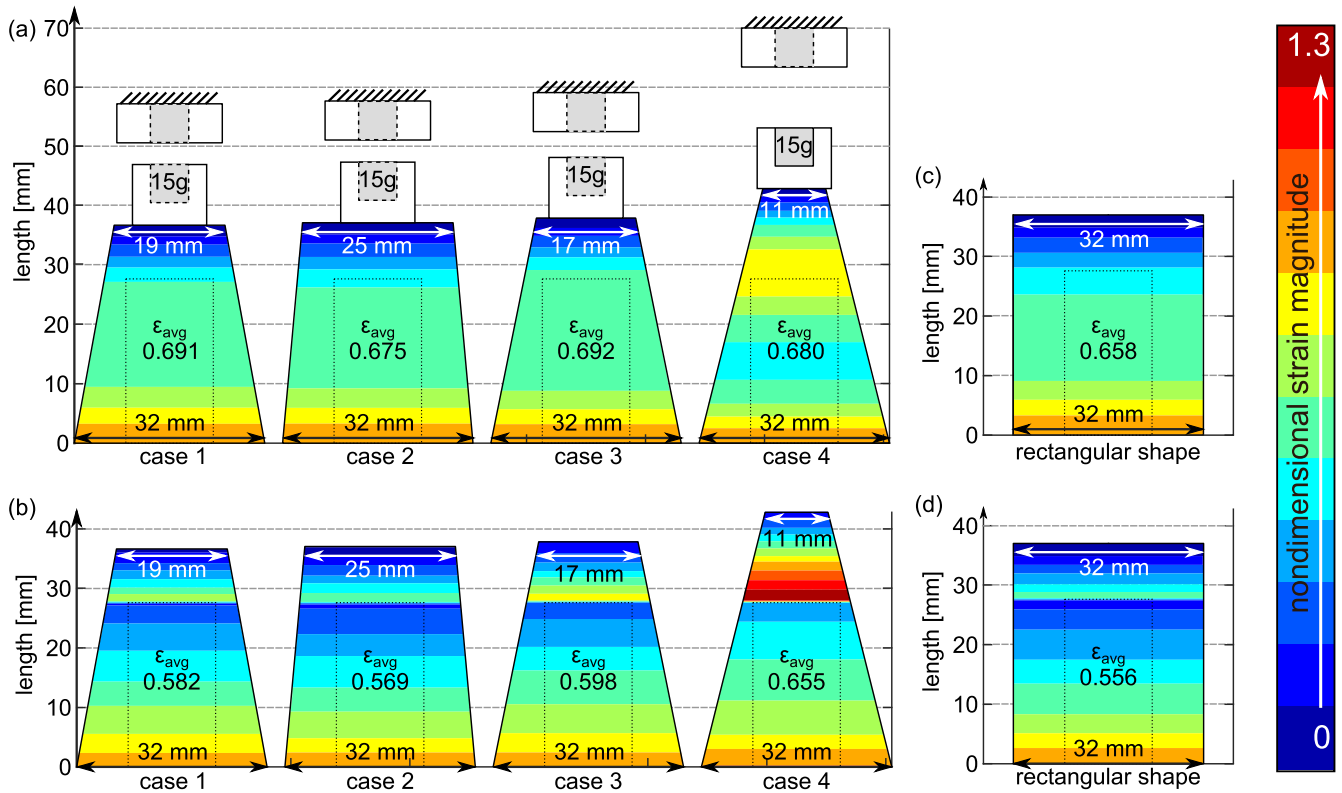


Figure 5. (a) Strain contour plot from analysis and (b) strain contour plot from finite element simulation of optimal designs. (c) Strain contour plot from analysis and (d) strain contour plot from finite element simulation of a rectangular shape for comparison.

cases are also referred to as cases 1, 2, 3, and 4 based on the weights used in the optimization.

The optimal designs obtained for the four cases including the beam length, beam width, and magnet gap are schematically shown in figure 5(a). The black dotted curve overlaid on each beam shape schematic is the outline of the piezoelectric layer. The grey squares represent the positions of the magnets, and the white rectangles are the magnet holders. The clamp location for the beams corresponds to the bottom of each respective schematic, so that the holder and magnet are installed at the opposite end. The repulsive magnets are positioned opposite of the magnet holder and the magnet gap is identified in the figure 5 according to the spacing shown. The mass labeled is the total tip mass, which is the combination of the magnet and the holder mass. The strain distribution of the cantilever on the bottom surface is also shown as the shaded contour in figure 5. The magnitude of the strain is nondimensionalized by the strain at the fixed end. The average values of the nondimensional strain ϵ_{avg} are reported on the surfaces and correspond to the average nondimensional strain over the area covered by the PZT-5H layer.

Figure 5(a) presents the analytical reconstruction of the strain distributions whereas figure 5(b) presents strain results obtained from finite element simulations (ABAQUS) of the piezoelectric cantilevers having the same optimized geometries, layering, and material properties. The schematics of the magnets in figure 5(b) are omitted for sake of brevity. Since in the analysis the strain is assumed to be uniform through the

beam width and equal to the axial strain, the finite element results are also presented with the axial strain mapped equally over the beam width. Here, both the analytical and finite element strain distribution for a rectangular beam shape are respectively provided in figures 5(c) and (d) for comparison. The dimensions of the rectangular beam include a constant beam width of 32 mm along the beam axis.

Comparing the finite element and analytical results in figures 5(a) and (b), the strain distribution around the end of the PZT cannot be exactly captured in the analysis due to the use of a limited number of trial functions. This is especially evident for case 4 in figure 5(a), where the finite element simulation figure 5(b) predicts a greater nondimensional strain at the position of the discontinuity than that suggested by the analysis in figure 5(a). Despite the relatively minor discrepancies, both analytical and finite element results demonstrate that a more uniform strain distribution is achieved over the tapered beam shape. The analysis and simulations both agree that the tapered beam strain distributions, figures 5(a) and (b), are more uniform when compared to the corresponding rectangular beams, figures 5(c) and (d). A greater average nondimensional strain over the piezoelectric layers indicates that the tapered beams deliver comparatively higher output electrical power to the loads than the rectangular beams. Therefore, considering the four cases of optimization, whether all objectives are equally weighted (case 1) or the individual objectives are set to be dominant (cases 2, 3, and 4), the optimization results show that tapered beams with strategic beam length and magnet gap

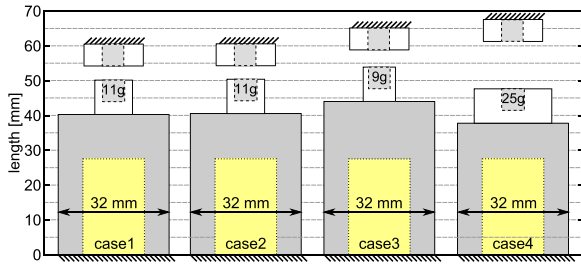


Figure 6. Optimal designs for optimization 3.

deliver improved global performance. When the strain condition (case 3) or rectified voltage (case 4) objective is dominant in the optimization, a higher taper ratio defined as b_L/b_0 is optimized. This further supports the conclusion that tapered beam shapes deliver higher power by the more uniform strain distribution, even though the piezoelectric layers only cover part of the beam. In addition, comparing with the optimal designs of cases 1 and 2, the magnet gap increases for the cases 3 and 4. This is especially evident for case 4, where the magnet gap is greatly increased to reduce nonlinearity and promote more linear response behavior. This agrees with the conclusion in section 4.2.1.

4.2.3. Optimization 3: beam length L , magnet gap d_2 , and tip mass M_0 . Since applications often envision collocation of the harvester with the powered microelectronics, it is desirable to limit the harvester mass to lead to a compact, lightweight energy harvesting platform for system integration. In the third optimization study, the beam length, magnet gap, and tip mass are taken as design parameters to optimize. Here a maximum tip mass 25 g is taken as additional constraint. Four cases with different weights setting as stated in section 4.2.1 are studied.

The optimal designs for the four cases are schematically shown in figure 6. As described in section 4.2.2, the light grey square and the white rectangle represent the magnet and the holder. The mass labels are the total magnet and holder mass. Since the extended length of the magnet holder at beam free end are constant, the shape or the material of the holder may change to ensure the optimal tip mass. In the schematics, the holder shape is changed to illustrate a change of optimized tip mass. The additional characteristics schematically shown in figure 6 are similar to those in figure 5. As first observed through the optimization of section 4.2.1, the magnet gap greatly increases for case 4 to promote linear dynamic behavior and greatest RMS voltage in a narrow frequency range. For the cases 1, 2, and 3 in figure 6, sufficient nonlinearity results from the repulsive magnet interaction to lead to a monostable configuration. Additionally, since the tip mass is directly related to the external force induced at the beam tip, when considering the tip mass as a design variable a larger mass corresponds to a greater tip force that increases the strain along the beam length and correspondingly delivers high output power. Therefore, when emphasizing the minimization of strain by case 3, the optimal design converges to a small tip mass shown in figure 6. In contrast, when the rectified output voltage becomes the dominant factor in the optimization shown by case 4, the maximum

allowable tip mass is selected with a short beam length to lead to a higher frequency of resonance, as similarly observed in section 4.2.1. For the cases 1 and 2, the optimized tip mass results from the respective balance of the multiple objectives in the cost function evaluations.

From the corresponding cost function values shown in figure 7, the change in the tip mass causes an up to 27 V change in the RMS voltage, while the RMS strain increases up to 900 $\mu\epsilon$ for case 4. This confirms the significant influence of the tip mass selection on the output voltage and strain at the cantilever fixed end. In contrast, the influence of tip mass on optimizing the frequency range is weak since the beam length and magnet gap are primarily shifted to promote a broader frequency range of the nonlinear resonant behavior. These results show that it is valuable to include the tip mass as a design variable in optimization to ensure that a combination of harvester design parameters is optimized having overall greatest lifetime and best power delivery.

From all optimal designs for case 4 in the three optimization problems considered in this section 4, when the voltage objective is dominant in the optimization extreme design conditions are reached. In other words, case 4 results in the maximum permitted beam length in optimization 2 and the maximum tip mass in optimization 3. The frequency responses of the optimal designs for the optimized results for case 4 are similar to linear responses, as seen by the examples in figures 4(d)–(f). Based on the narrowband resonant behavior, such linear systems may easily lose superiority of performance when excitation conditions change. Therefore, in an optimization of an energy harvesting system, a strict optimization on the basis of maximizing output voltage is not recommended. Comparatively, preferring optimizing on the basis of frequency range, strain at the fixed beam end, or the more balanced multi-objective optimization lead to robust energy harvesters that may serve in practical environments.

5. Experimental system description

The key findings from the analytical model and optimization investigations are then validated through controlled experiments. Based on the optimal designs of the laminated piezoelectric cantilevers determined through cases 1–3 in section 4.2, three beams shown in figure 8(a) are cut from off-the-shelf piezoelectric energy harvesters by Midé Technology. The shapes are cut using a CNC router. Due to limitations of creating the cut-out cantilever shapes, the optimal geometries are unable to be exactly achieved although they are closely emulated. The beams 1, 2, and 3 shown in figure 8(a) have experimentally identified parameters given in table 4, while the remaining parameters not given are provided in table 2.

Figure 8(b) presents the experimental setup used to examine the three piezoelectric cantilevers. For each experiment, the piezoelectric beam is clamped to an aluminum frame mounted to an electrodynamic shaker table (APS Dynamics 400). At the free end of the piezoelectric beam, an aluminum magnet holder is installed. An opposing magnet holder is affixed to the shaker table at a location immediately adjacent to the beam tip along the

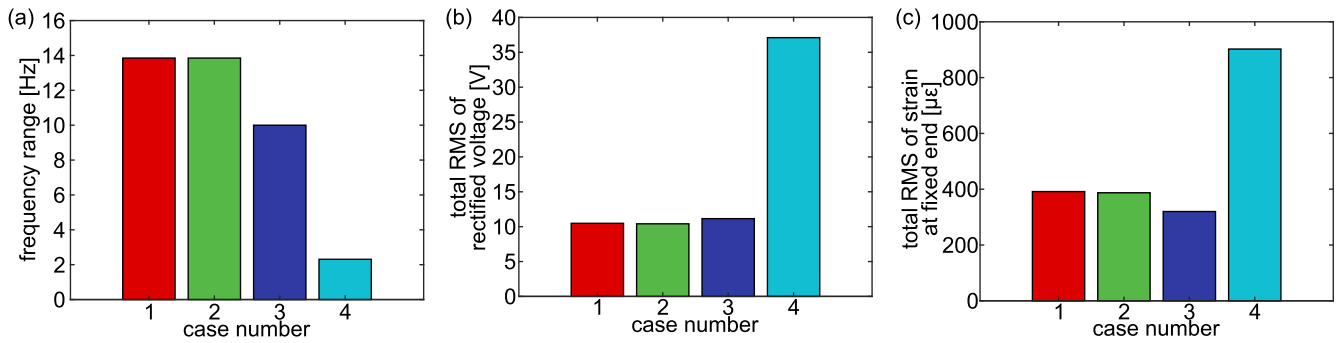


Figure 7. Cost function values of four optimal designs. (a) Frequency range. (b) Total RMS of the output voltage. (c) Total RMS of the strain at the fixed end.

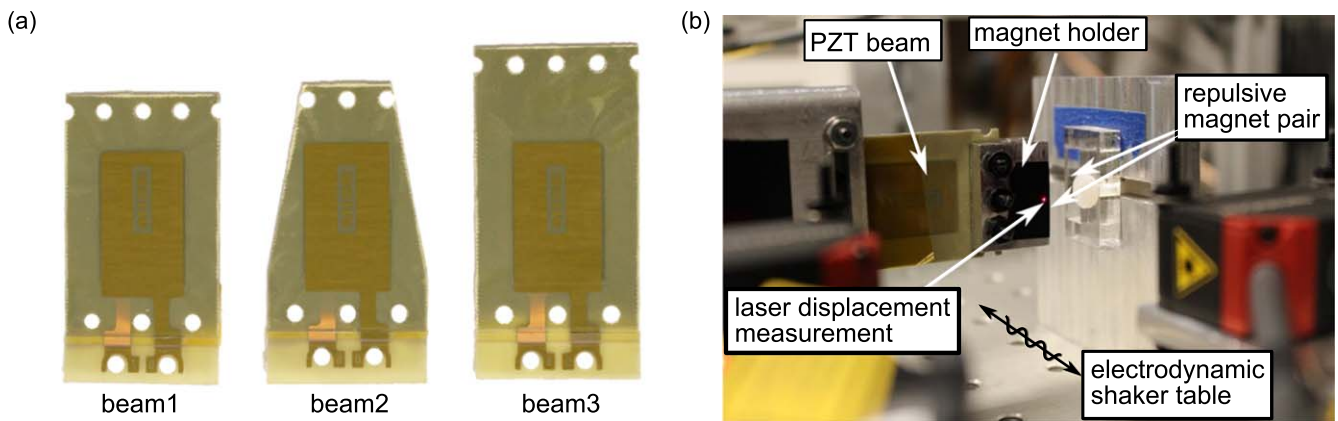


Figure 8. (a) Three beams shapes for experiments. (b) Photograph of the experiment platform.

Table 4. Parameters for three beams identified from experiments.

	L (mm)	b_L (mm)	h_s (mm)	h_c (mm)	d_2 (mm)		ϵ_{33} (nF m ⁻¹)	e_{31} (C m ⁻²)	M_0 (g)
					Monostable case	Bistable case			
Beam 1	37.4	32	0.034	0.02	10.8	10.4	30.15	-14.54	16.6
Beam 2	37.4	18	0.04	0.02	10.6	10.3	30.15	-14.54	16.6
Beam 3	45	32	0.034	0.02	11.8	11.6	30.15	-14.54	7.0

beam axis, as shown in figure 8(b). The shaker table is driven by a controller (Vibration Research Controller VR9500) and amplifier (Crown XLS 2500) with an accelerometer (PCB Piezotronics 333B40) to provide control signal feedback to ensure the base acceleration amplitude remains 5 m s^{-2} at all frequencies examined. Two laser displacement sensors (Micro-Epsilon ILD-1420) measure the absolute displacement of the beam tip and the shaker table. A bridge rectifier (1N4148 diodes) with a smoothing capacitor C_r and resistive load R are connected to the piezoelectric beam to quantify the converted electric energy.

6. Experiment validation

The experiments examine both monostable and bistable configurations of beams 1, 2, and 3. Figures 9(a) and (b) respectively show the displacement amplitude of the beam tip and rectified output voltage of the three beams for a

monostable configuration. Figures 9(d) and (e) are the corresponding responses for a bistable configuration of each beam. Analytical predictions are shown as the thick curves whereas the experimental results are presented using thin curves in the same respective line style. Because the strain at the clamped ends of the beams cannot be measured without influencing the laminated beam mechanical properties, the strain responses shown in figures 9(c) and (f) are calculated from finite element analysis (FEA) using ABAQUS. In the FEA, a solid model of the exact beam composition is used, where all parameters employed are provided in tables 2 and 4. Rigid elements are included to model the aluminum magnet holder, and a mass element is used to model the beam tip mass. After establishing the finite element model, the displacement amplitudes shown in figures 9(a) and (d) are applied as boundary conditions for the FEA to compute a static load analysis that provides values of the clamped end strain, using the strain at the middle of the clamp.

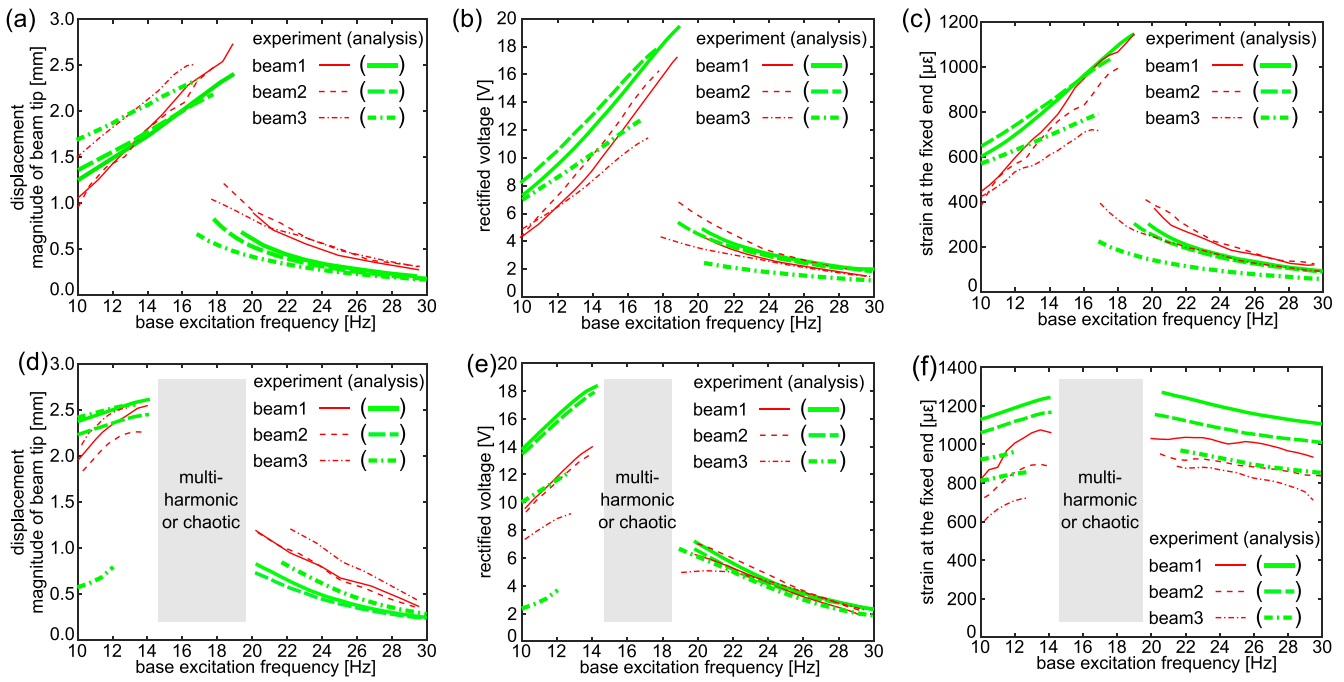


Figure 9. Frequency responses for three beams. (a) Displacement amplitude at the beam tip, (b) rectified output voltage, and (c) strain at the fixed end for monostable configurations. (d)–(f) Corresponding responses for bistable configuration.

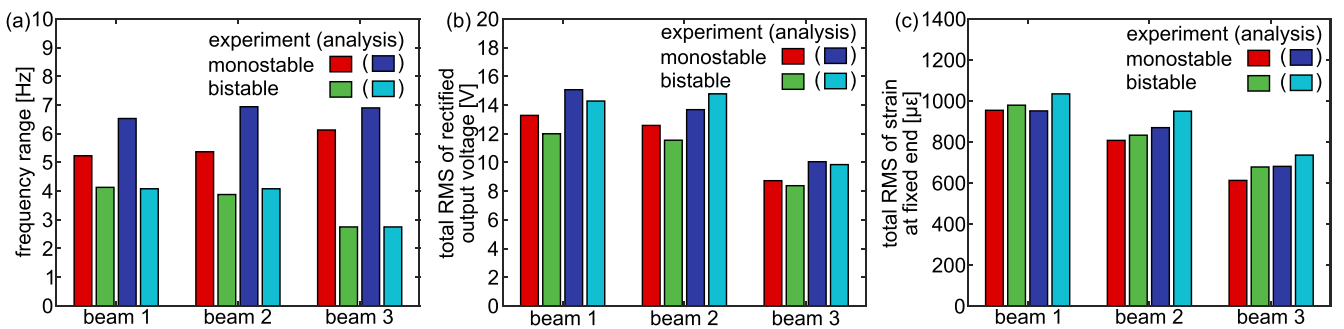


Figure 10. Comparison of cost function values between experiment and analysis for three beam designs. (a) Frequency range. (b) Total RMS of the rectified output voltage. (c) Total RMS of the strain at the fixed end.

From the displacement responses shown in figures 9(a) and (d), the large displacement amplitudes at the bifurcations are in good agreement between the analysis and experimentation. Since the stiffness of the beam is increased due to the rigid cross-section assumption in Euler–Bernoulli beam theory, the analytical strain predictions in figures 9(c) and (f) are relatively greater than the FEA results using the experimental data of displacement amplitude. This in turn increases the predicted analytical output voltage in figures 9(b) and (e) compared to the experimental levels. Electrical component losses and higher order harmonics are also neglected in analysis, which may also contribute to the overprediction of rectified voltage. The grey shaded areas in figures 9(d)–(f) correspond to multi-harmonic or chaotic dynamic behaviors that are not predicted by analysis due to steady-state assumptions in the solution formulation. Despite these discrepancies, the overall quantitative agreement between the experimental and analytical results in figure 9 exemplifies that the model formulation accurately replicates the

electromechanical behaviors of the piezoelectric laminated energy harvester.

The results of figure 10 establish the efficacy of the optimization created through this research. The results of monostable cases of all three beams suggest a higher output voltage with a lower strain level and a wider frequency range (red or blue bars) when compared to the bistable configurations of the energy harvesters (green or cyan bars). This emphasizes the global superiority of monostable platforms over bistable system configurations to achieve broadly robust energy harvesting performance and agrees with results obtained throughout section 4. In addition, the tapered beam 2 exhibits quantitatively less strain at the clamped end than the rectangular beam 1 of the same length, figure 10(c), while the beam 2 is within 1 V RMS of the rectified output voltage of beam 1, figure 10(b). This result agrees with the findings of section 4.2.2. Furthermore, when the tip mass decreases to 7 g for beam 3, the frequency range may still be broad by

introducing sufficient nonlinearity as shown in figure 10(a). Yet, the output voltage and strain for beam 3 in figures 10(b) and (c) are decreased comparing with the results of the other two beams, which supports the influences uncovered in section 4.2.3. Thus, considering the design constraints examined here, piezoelectric laminated cantilevers with tapered shapes, monostable nonlinearity, and moderate lengths deliver the most performance robust DC power delivery.

7. Conclusions


This research provides the first illumination of the coupled influences of nonlinearity and beam shape design on the resulting mechanical robustness and versatile electrical power generation of a nonlinear energy harvesting system. Here, an analytical model is established and verified through numerical simulations and experimental examinations for key influences of nonlinearity, beam shape, and tip mass select result in robust system designs. Multi-objective optimization guides attention to strategic combinations of design parameters based on the specific optimization variables and relative weights given to the objective functions. Trapezoidal beam shapes are found to promote large output voltage without yielding high strain at the clamped end, which promotes practical longevity of the system. Bistable implementations of the nonlinear energy harvesters are found to be undesirable for sake of large residual strain at the clamped end, even though they may deliver wide frequency range of operation and high output voltages. Therefore, both the optimization results using the new analysis and experiment validations indicate that a trapezoidal beam in a monostable configuration is globally preferred.

Acknowledgments

This research is supported by the National Science Foundation under Award No. 1661572. The authors are grateful to hardware support from Midé Technology.

ORCID iDs

Wen Cai  <https://orcid.org/0000-0002-7274-9884>

Ryan L Harne  <https://orcid.org/0000-0003-3124-9258>

References

- [1] Magno M, Spadaro L, Singh J and Benini L 2016 Kinetic energy harvesting: toward autonomous wearable sensing for internet of things *2016 Int. Symp. on Power Electronics, Electrical Drives, Automation and Motion (Anacapri)* pp 248–54
- [2] Evans D 2011 The internet of things: how the next evolution of the internet is changing everything *CISCO White Pap.* **1** 1–11
- [3] Jayakumar H, Lee K, Lee W S, Raha A, Kim Y and Raghunathan V 2014 Powering the internet of things *Proc. 2014 Int. Symp. on Low Power Electronics and Design (La Jolla)* pp 375–80
- [4] Gorlatova M, Sarik J, Grebla G, Cong M, Kymissis I and Zussman G 2014 Movers and shakers: kinetic energy harvesting for the Internet of things *ACM SIGMETRICS Perform. Eval. Rev.* **42** 407–19
- [5] Cho J, Anderson M, Richards R, Bahr D and Richards C 2005 Optimization of electromechanical coupling for a thin-film PZT membrane: I. Modeling *J. Micromech. Microeng.* **15** 1797
- [6] Wang Q and Wu N 2012 Optimal design of a piezoelectric coupled beam for power harvesting *Smart Mater. Struct.* **21** 085013
- [7] Lü C, Zhang Y, Zhang H, Zhang Z, Shen M and Chen Y 2019 Generalized optimization method for energy conversion and storage efficiency of nanoscale flexible piezoelectric energy harvesters *Energy Convers. Manage.* **182** 34–40
- [8] Qin L, Jia J, Choi M and Uchino K 2019 Improvement of electromechanical coupling coefficient in shear-mode of piezoelectric ceramics *Ceram. Int.* **45** 1496–502
- [9] Baker J, Roundy S and Wright P 2005 Alternative geometries for increasing power density in vibration energy scavenging for wireless sensor networks *3rd Int. Energy Conversion Engineering Conf. (San Francisco)* pp 2005–5617
- [10] Hosseini R and Hamed M 2015 Improvements in energy harvesting capabilities by using different shapes of piezoelectric bimorphs *J. Micromech. Microeng.* **25** 125008
- [11] Roundy S *et al* 2005 Improving power output for vibration-based energy scavengers *IEEE Pervasive Comput.* **1** 28–36
- [12] Montazer B and Sarma U 2018 Design and optimization of quadrilateral shaped PVDF cantilever for efficient conversion of energy from ambient vibration *IEEE Sens. J.* **18** 3977–88
- [13] Tabatabaei S M K, Behbahani S and Rajaeipour P 2016 Multi-objective shape design optimization of piezoelectric energy harvester using artificial immune system *Microsyst. Technol.* **22** 2435–46
- [14] Matova S P, Renaud M, Jambunathan M, Goedbloed M and Van Schaijk R 2013 Effect of length/width ratio of tapered beams on the performance of piezoelectric energy harvesters *Smart Mater. Struct.* **22** 075015
- [15] Dietl J M and Garcia E 2010 Beam shape optimization for power harvesting *J. Intell. Mater. Syst. Struct.* **21** 633–46
- [16] Raju S S, Umapathy M and Uma G 2018 High-output piezoelectric energy harvester using tapered beam with cavity *J. Intell. Mater. Syst. Struct.* **29** 800–15
- [17] Xu J W, Liu Y B, Shao W W and Feng Z 2012 Optimization of a right-angle piezoelectric cantilever using auxiliary beams with different stiffness levels for vibration energy harvesting *Smart Mater. Struct.* **21** 065017
- [18] Yoon H S, Washington G and Danak A 2005 Modeling, optimization, and design of efficient initially curved piezoceramic unimorphs for energy harvesting applications *J. Intell. Mater. Syst. Struct.* **16** 877–88
- [19] Chandrasekharan N and Thompson L L 2016 Increased power to weight ratio of piezoelectric energy harvesters through integration of cellular honeycomb structures *Smart Mater. Struct.* **25** 045019
- [20] Harne R L and Wang K W 2017 *Harnessing Bistable Structural Dynamics: for Vibration Control, Energy Harvesting and Sensing* (Chichester: Wiley)
- [21] Cottone F, Vocca H and Gammaitoni L 2009 Nonlinear energy harvesting *Phys. Rev. Lett.* **102** 080601
- [22] Harne R L and Wang K W 2013 A review of the recent research on vibration energy harvesting via bistable systems *Smart Mater. Struct.* **22** 023001
- [23] Erturk A, Hoffmann J and Inman D J 2009 A piezomagnetoelastic structure for broadband vibration energy harvesting *Appl. Phys. Lett.* **94** 254102

- [24] Ferrari M, Ferrari V, Guizzetti M, Andò B, Baglio S and Trigona C 2010 Improved energy harvesting from wideband vibrations by nonlinear piezoelectric converters *Sensors Actuators A* **162** 425–31
- [25] Nguyen M S, Yoon Y J, Kwon O and Kim P 2017 Lowering the potential barrier of a bistable energy harvester with mechanically rectified motion of an auxiliary magnet oscillator *Appl. Phys. Lett.* **111** 253905
- [26] Yang W and Towfighian S 2018 Low frequency energy harvesting with a variable potential function under random vibration *Smart Mater. Struct.* **27** 114004
- [27] Hosseinloo A H and Turitsyn K 2015 Non-resonant energy harvesting via an adaptive bistable potential *Smart Mater. Struct.* **25** 015010
- [28] Zhou Z, Qin W, Du W, Zhu P and Liu Q 2019 Improving energy harvesting from random excitation by nonlinear flexible bi-stable energy harvester with a variable potential energy function *Mech. Syst. Signal Process.* **115** 162–72
- [29] Panyam M and Daqaq M F 2017 Characterizing the effective bandwidth of tri-stable energy harvesters *J. Sound Vib.* **386** 336–58
- [30] Lai S K, Wang C and Zhang L H 2019 A nonlinear multi-stable piezomagnetoelastic harvester array for low-intensity, low-frequency, and broadband vibrations *Mech. Syst. Signal Process.* **122** 87–102
- [31] Dai Q and Harne R L 2018 Investigation of direct current power delivery from nonlinear vibration energy harvesters under combined harmonic and stochastic excitations *J. Intell. Mater. Syst. Struct.* **29** 514–29
- [32] Cai W and Harne R L 2018 Electrical power management and optimization with nonlinear energy harvesting structures *J. Intell. Mater. Syst. Struct.* **30** 213–27
- [33] Avvari P V, Yang Y and Soh C K 2017 Long-term fatigue behavior of a cantilever piezoelectric energy harvester *J. Intell. Mater. Syst. Struct.* **28** 1188–210
- [34] Upadrashta D, Yang Y and Tang L 2015 Material strength consideration in the design optimization of nonlinear energy harvester *J. Intell. Mater. Syst. Struct.* **26** 1980–94
- [35] Pandey A and Arockiarajan A 2017 An experimental and theoretical fatigue study on macro fiber composite (MFC) under thermo-mechanical loadings *Eur. J. Mech. A* **66** 26–44
- [36] Gundimeda S K, Kunc S, Gallagher J A and Fragoudakis R 2018 Simulation of a composite piezoelectric and glass fiber reinforced polymer beam for adaptive stiffness applications *ASME 2018 Conf. on Smart Materials, Adaptive Structures and Intelligent Systems. American Society of Mechanical Engineers (San Antonio)* V001T03A025
- [37] Li X, Upadrashta D, Yu K and Yang Y 2018 Sandwich piezoelectric energy harvester: analytical modeling and experimental validation *Energy Convers. Manage.* **176** 69–85
- [38] Harne R L and Wang K W 2016 Axial suspension compliance and compression for enhancing performance of a nonlinear vibration energy harvesting beam system *J. Vib. Acoust.* **138** 011004
- [39] Goldschmidtboeing F and Woias P 2008 Characterization of different beam shapes for piezoelectric energy harvesting *J. Micromech. Microeng.* **18** 104013
- [40] Hagood N W, Chung W H and Von Flotow A 1990 Modelling of piezoelectric actuator dynamics for active structural control *J. Intell. Mater. Syst. Struct.* **1** 327–54
- [41] Lan C, Tang L and Harne R L 2018 Comparative methods to assess harmonic response of nonlinear piezoelectric energy harvesters interfaced with AC and DC circuits *J. Sound Vib.* **421** 61–78
- [42] Jaworski J W and Dowell E H 2008 Free vibration of a cantilevered beam with multiple steps: comparison of several theoretical methods with experiment *J. Sound Vib.* **312** 713–25
- [43] Spanos P D 1981 Stochastic linearization in structural dynamics *Appl. Mech. Rev.* **34** 1–8
- [44] Atalik T S and Utku S 1976 Stochastic linearization of multi-degree-of-freedom non-linear systems *Earthq. Eng. Struct. Dyn.* **4** 411–20
- [45] Liang J and Liao W H 2012 Impedance modeling and analysis for piezoelectric energy harvesting systems *IEEE/ASME Trans. Mechatronics* **17** 1145–57
- [46] Liao Y and Liang J 2019 Unified modeling analysis and comparison of piezoelectric vibration energy harvesters *Mech. Syst. Signal Process.* **123** 403–25
- [47] Meier R, Kelly N, Almog O and Chiang P 2014 A piezoelectric energy-harvesting shoe system for podiatric sensing *2014 36th Annual Int. Conf. of the IEEE Engineering in Medicine and Biology Society (EMBC) (Chicago)* pp 622–5
- [48] Haupt R L and Haupt S E 2004 *Practical Genetic Algorithms* (New York: Wiley)
- [49] Dai Q and Harne R L 2017 Charging power optimization for nonlinear vibration energy harvesting systems subjected to arbitrary, persistent base excitations *Smart Mater. Struct.* **27** 015011
- [50] Zheng Q and Xu Y 2008 Asymmetric air-spaced cantilevers for vibration energy harvesting *Smart Mater. Struct.* **17** 055009
- [51] Erturk A and Inman D J 2011 Broadband piezoelectric power generation on high-energy orbits of the bistable Duffing oscillator with electromechanical coupling *J. Sound Vib.* **330** 2339–53
- [52] Harne R L and Goodpaster B A 2018 Impedance measures in analysis and characterization of multistable structures subjected to harmonic excitation *Mech. Syst. Signal Process.* **98** 78–90